Geophys. J. Int. (1999) **138**, 809–819

Determination of the crustal structure in southern Tibet by dispersion and amplitude analysis of Rayleigh waves

N. Cotte,[1] H. Pedersen,[1] M. Campillo,[1] J. Mars,[2] J. F. Ni,[3] R. Kind,[4] E. Sandvol[5] and W. Zhao[6]

[1] *Laboratoire de Géophysique Interne et Tectonophysique, Observatoire de Grenoble, Université Joseph Fourier, Grenoble, France. E-mail: ncotte@obs.ujf-grenoble.fr*
[2] *Centre d'Etude des Phénomènes Aléatoires et Géophysiques, Observatoire de Grenoble, Université Joseph Fourier, Grenoble, France*
[3] *Department of Physics, New Mexico State University, Las Cruces, USA*
[4] *GeoForschungsZentrum Potsdam, Telegrafenberg,* 14473 *Potsdam, Germany*
[5] *Department of Geological Sciences, Cornell University, Ithaca, USA*
[6] *Chinese Academy of Geological Sciences, Beijing, China*

Accepted 1999 April 20. Received 1998 December 10; in original form 1998 March 20

SUMMARY

Surface waves recorded by the nine broad-band stations of the INDEPTH II experiment are analysed to study the crustal structure of southern Tibet. Their frequency range is between approximately 0.015 and 0.050 Hz (i.e. between 20 and 60 s period). Phase velocity dispersion curves are calculated for the regions north and south of the Tsangpo suture, using Wiener filtering of fundamental mode Rayleigh waves incident upon the array with different backazimuths. The two dispersion curves are inverted to obtain the *S*-wave crustal models north and south of the suture. They show that a low-velocity layer is present in the lower crust north but not south of the Tsangpo suture. To confirm these findings, variations in the amplitudes of the Rayleigh waves across the suture are interpreted by numerical simulation. The strong amplitude variations at a 30 s period are reproduced using a model with a low-velocity layer in the lower crust north of the suture, a normal high-velocity layer to the south, and a sharp transition between these layers.

Key words: amplitude variations, dispersion, Rayleigh waves, southern Tibet, surface waves.

INTRODUCTION

The archetypal example of an active continent–continent collision is that between Asia and India, which began at about 50 Ma and continues today, raising the Himalayan range and the Tibetan plateau (e.g. McKenzie & Sclater 1971; Molnar & Tapponnier 1975). The Himalayas are the highest range on Earth, whilst Tibet has an average altitude of 5000 m and is underlain by anomalously thick crust, approximately twice the thickness of 'normal' continental crust.

Heterogeneities in the crustal thickness and lithospheric velocity of the Tibetan plateau were identified by studying surface waves. Romanowicz (1982) measured event–station phase delays for pairs of events in order to study the area between them. Tomographic images have also been used, with either surface or *Pn* waves, to demonstrate velocity anomalies (Bourjot & Romanowicz 1992; Wittlinger *et al.* 1996; McNamara *et al.* 1997; Wu *et al.* 1997). Levshin *et al.* (1994) used the polarization anomalies of surface waves to determine the structure in central Eurasia, and, more recently, Curtis & Woodhouse (1997) calculated interevent surface wave phase velocities in order to find lithospheric models for Tibet. All these studies provide large-scale velocity models of the lithosphere beneath the Tibetan plateau, but little information on variations inside the plateau.

Other types of seismological studies have revealed strong lateral variations within the plateau. For example, anisotropy and crustal thickness vary on a small scale (McNamara *et al.* 1997; Ni & Barazangi 1983; Guilbert *et al.* 1996; Hirn *et al.* 1995; Sandvol *et al.* 1997), and *Lg*-wave propagation also varies within the plateau (McNamara *et al.* 1996). Several studies have determined the *S*-wave structure with variations inside the plateau (e.g. Curtis & Woodhouse 1997), and Yuan *et al.* (1997) have demonstrated lateral crustal variations in southern Tibet using a receiver function analysis.

The analysis of surface waves recorded by densely spaced stations makes it possible to study variations in *S*-wave velocity on a regional scale. The INDEPTH II experiment was the

first very densely spaced broad-band array within the Tibetan plateau. The purpose of this experiment (Nelson *et al.* 1996) was to investigate the structure of the lithosphere beneath the southern part of the Tibetan plateau and across the Tsangpo suture, which separates the Asian and Indian plates. The experiments carried out during 6 months in 1994 within INDEPTH II included both active and passive seismic experiments using broad-band and short-period stations.

There are two main results from the INDEPTH II experiments. The first is the existence of bright spots, observed both in the seismic reflection profiles (Makovsky *et al.* 1996; Brown *et al.* 1996) and by magnetotelluric surveying (Chen *et al.* 1996). The existence of these bright spots was discussed by Zhao *et al.* (1997) in terms of tectonics. The second result, which appears to be the cause of the bright spots, is evidence of partial melt in the middle crust, which may be related to the shortening of the Asian plate (Nelson *et al.* 1996; Kind *et al.* 1996; Reese & Ni 1996). Such a layer has also been determined by other experiments (e.g. Hirn *et al.* 1997). Kind *et al.* (1996) identified it using surface wave analysis across the INDEPTH II array, but their study was based on a single teleseismic event.

In the current work, we analyse surface waves from several seismic events to determine phase velocities independently north and south of the suture. We also analyse variations in the amplitude of the Rayleigh wave fundamental mode across the suture. These amplitude anomalies cannot be interpreted directly, but we show by numerical simulations that they are consistent with the crustal model obtained by the phase velocity analysis.

DATA SELECTION

Our goal is to determine the *S*-wave velocity structure north and south of the Tsangpo suture. The frequency contents of the surface waves recorded by the broad-band stations of the INDEPTH II experiment are approximately between 0.015 and 0.050 Hz (i.e. between 20 and 60 s period), thus making it possible to study the crustal structure. During the 6 months of the experiment, nine broad-band stations equipped with Guralp CMG-3T seismometers were installed along a line crossing the suture, almost perpendicular to it. As shown in Fig. 1, four of the broad-band stations were located north of the suture, four were located south of it and one was located on it. The length of the profile was approximately 200 km. The station locations are listed in Table 1.

Only teleseismic events are used here, to ensure that surface waves are well separated from body wave arrivals. Events with an incidence from both the north and the south and with a good signal to noise ratio between 20 and 60 s period are

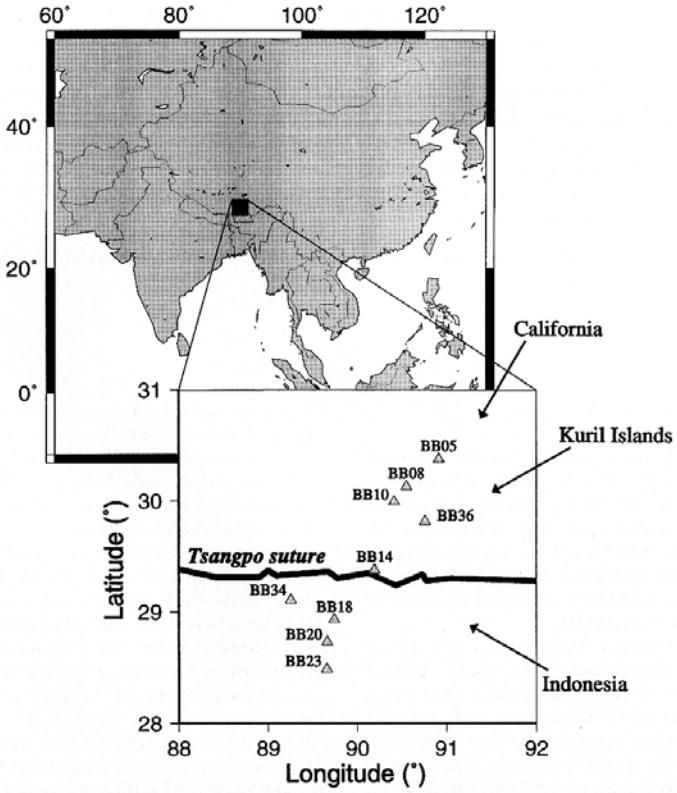

Figure 1. Locations of the broad-band stations used in the INDEPTH II experiment in southern Tibet. Black arrows show the arrival directions of surface waves from the three events used in the analysis.

Table 1. Locations of the broad-band stations of the INDEPTH II experiment. Stations BB05, BB08, BB10 and BB36 are located north of the Tsangpo suture; station BB14 is located on the suture; stations BB18, BB20, BB23 and BB34 are located south of the suture (see Fig. 1).

Station	Longitude E	Latitude N
BB05	90.911°	30.379°
BB08	90.548°	30.130°
BB10	90.413°	29.991°
BB14	90.191°	29.376°
BB18	89.742°	28.930°
BB20	89.663°	28.728°
BB23	89.659°	28.486°
BB34	89.256°	29.108°
BB36	90.757°	29.816°

selected. Records of the vertical component filtered between 0.01 and 0.10 Hz are shown for three of these events, which will later be used in the amplitude analysis (Fig. 2). The backazimuths of the three events are indicated in Fig. 1 by arrows. For each event, the records in Fig. 2 are sorted by epicentral distance, that is, from northeast to southwest for the Californian and Kuril Islands events and from southeast to northwest for the Indonesian event. The amplitudes of the records are normalized to increase clarity, but relative amplitudes between stations are respected for each event. Note that the dominant phase is the Rayleigh fundamental mode.

DATA PROCESSING AND ANALYSIS

The data analysis is performed in two ways. First, the phase velocities are calculated independently north and south of the Tsangpo suture and the two dispersion curves are inverted to obtain *S*-wave velocity variations with depth. Second, the spectral amplitude variations are measured across the array for the three events of Fig. 2.

Phase velocity analysis

The aim of this part of the study is to determine the shear wave velocity structure north and south of the Tsangpo suture independently. Only one event (the Californian event, see Fig. 1) is available with a great-circle path approximately aligned with the profile. Consequently, it is difficult to estimate errors on the phase velocity measurements using only this single event. An additional problem is that the Californian event shows significant polarization anomalies across the array.

We therefore considered all teleseismic events for which at least one pair of stations on the same side of the suture was located approximately on the great-circle path through the epicentre. For example, surface waves from the Kuril Islands are incident with a 5° difference from the great-circle path between stations BB05 and BB08, and with an 8° difference from the great-circle path between stations BB36 and BB14. The small distances between the stations (e.g. 45 km between BB05 and BB08 and 74 km between BB36 and BB14) and the shift between the interstation and great-circle paths to the epicentre (up to 10°) make the uncertainties on the phase velocity measurements rather large. On the other hand, we

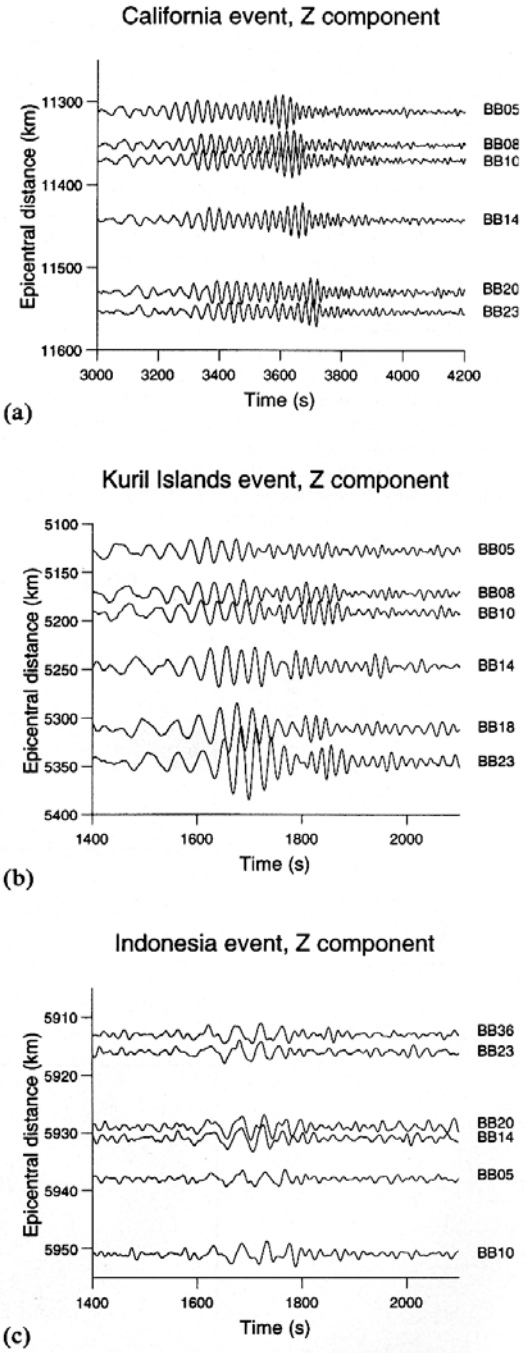

Figure 2. Vertical component of the fundamental mode of the Rayleigh wave recorded for three events. Top: Californian event; middle: Kuril Islands event; bottom: Indonesian event.

use three different backazimuths in our measurements with the Californian, five Kuril Islands, and Indonesian events. The Indonesian event provides some assurance that no systematic bias is introduced in the measurements as its incidence is from the southeast.

The phase velocities are measured by Wiener filtering (Wiener 1949; see also Nakanishi 1979, Taylor & Toksöz 1982 and Hwang & Mitchell 1986) performed in the frequency domain. The advantage of Wiener filtering as compared to measuring the phase difference of smoothed spectra is the minimization of the influence of random noise. Phase velocities are only measured for frequencies with a coherence greater than 0.9.

The phase velocities north and south of the Tsangpo suture are shown in Fig. 3(a). Although the scatter is significant, the two curves tend to be of a different shape. North of the suture, the phase velocity is constant between 20 and 40 s period, and increases between 40 and 60 s, whereas to the south the phase velocity increases over the whole period interval of 20–60 s. This difference reveals that the crustal structure is not the same north and south of the suture. However, the large scatter in the measurements makes it crucial to investigate whether models for which the phase velocity dispersion curve falls within the observed phase velocities north and south of the suture are significantly different. To this end, we adapted the two-step inversion method suggested by Shapiro *et al.* (1997).

The two average dispersion curves and their standard deviations were calculated using the following procedure. (1) The average dispersion curve was inverted through a classical, linearized dispersion scheme (e.g. Herrmann 1987) to find the simplest possible shear wave model for which the theoretical dispersion curve fits the observations. The choice to search for a model with a small number of layers is to ensure that the solution is stable, and not a secondary minimum. In this simple configuration, the final velocity models were similar for very different starting models. The downside of our procedure is the neglect of models with a rapidly varying velocity structure, or with a smooth velocity gradient, but such a model would not be resolved by the data. (2) Random variations were then applied to this 'average' model to obtain a set of possible models, out of which we retained those for which the theoretical dispersion curve fell within the standard deviation of the observed one. This second step was repeated 1000 times to give a large population of models with theoretical dispersion

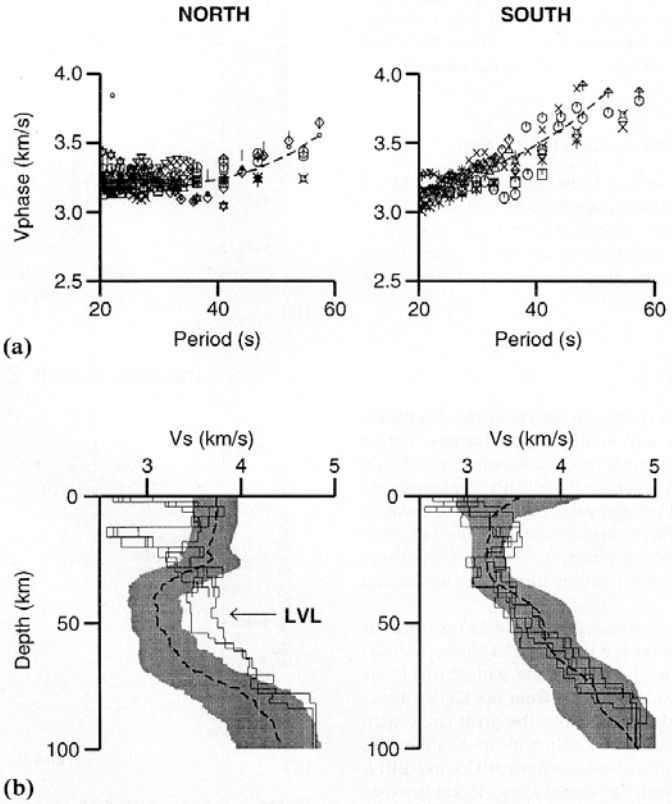

Figure 3. (a) Phase velocity dispersion curves calculated from INDEPTH II data. Dashed line: average velocity. (b) Models of shear wave velocity variations with depth obtained by inversion of phase velocities north (left) and south (right) of the Tsangpo suture. Dashed line: average velocity model. The grey shaded zone shows the range of shear wave velocity models compatible with the measured dispersion curves. The results provided by the receiver function method (Yuan *et al.* 1997) are plotted as thin black lines (1 model for each station).

curves fitting the observation within the uncertainties of measurement. Finally, average and standard deviations of the population were calculated.

Fig. 3(b) shows the result of this analysis applied to the two observed dispersion curves plotted as shaded zones. Whilst possible differences in the upper crustal structure are not resolved, a low-velocity layer is present in the lower crust north of the Tsangpo suture, but no such layer appears to be present south of it. Superimposed onto the two models are the results of the receiver function analysis conducted on each of the broad-band stations of the INDEPTH II experiment by Yuan *et al.* (1997).

The fit between our models and those obtained by the receiver function analysis is very good south of the suture, whereas to the north the results are very different. The receiver function models show a thin, very strong low-velocity layer at 15–20 km depth, whilst our analysis shows a thick low-velocity layer in the lower crust.

This apparent discrepancy can be explained by taking the resolution capacity of the two methods into account. Due to the sampling of surface waves over quite large depth intervals, the surface wave analysis gives a good estimate of the overall velocity profile in the crust, but does not resolve a thin low-velocity layer in the upper crust. Our average model still agrees with the observed dispersion curve even after adding a thin low-velocity layer in the upper crust. On the other hand, the receiver functions north of the suture are dominated by the thin low-velocity layer which is well resolved by this method. However, the presence of such a layer at a shallow depth significantly decreases the resolution of the receiver function analysis in the lower crust because the shallow low-velocity layer creates reverberations that mask converted phases from deeper crustal velocity variations. Note that only two out of the five receiver function models computed at stations located north of the suture extend beyond 40 km depth. The surface wave models, on the other hand, are well resolved in the lower crust. We verified this by using different starting models in the second step of the inversion procedure, for example by using the average 'north' model as input to the 'south' inversion and vice versa. We also tested the influence of layer thicknesses and upper crustal velocities.

The surface wave analysis therefore reveals a significant change in the lower crustal structure across the suture, with the presence of a low-velocity layer in the lower crust north of it and no such layer south of it. In the next subsection we show how this interpretation is supported by the analysis of spectral amplitudes of the surface waves.

Spectral amplitude variations across the Tsangpo suture

A difference in the crustal structure north and south of the Tsangpo suture as described above may induce amplitude variations across the suture. Such amplitude variations are clearly present on the record of the Kuril Islands event (see Fig. 2) but a spectral analysis is necessary to determine whether such variations are present for other events, and in which frequency range.

In Fig. 1, the backazimuths of the three events used for the spectral analysis are shown as black arrows. The locations of these events are given in Table 2. Surface waves from the Californian and Kuril Islands events are incident from the northeast with backazimuths of approximately 30° and 60° respectively. Surface waves from the Indonesian event are incident from the south with a backazimuth of approximately 120°.

For these three events a spectral analysis was performed, with the purpose of studying amplitude variations across the array. Seismograms were selected between 3000 and 3800 s for the Californian event, between 1425 and 1975 s for the Kuril Islands event and between 1500 and 1900 s for the Indonesian event (see Fig. 2). Figs 4(a), (c) and (e) show spectral amplitudes of the Rayleigh fundamental mode between 0.02 and 0.05 Hz (i.e. between 20 and 50 s period) for the vertical component of these events. For each event, the spectra are normalized by the maximum amplitude between 0.030 and 0.036 Hz (shown by grey shading). Consequently, the relative amplitude between stations for the same event is respected.

The Californian event (Fig. 4a) shows a nearly constant amplitude level across the array and in the whole frequency range. The main lateral change in amplitude is observed for the Kuril Islands event (Fig. 4c) between 0.030 and 0.036 Hz (i.e. approximately 30 s period), for which the spectral amplitudes increase steadily across the array from north to south. The amplitude ratio between stations BB23 and BB14 is 1.7 at 0.033 Hz. We also observe a similar amplitude anomaly in this frequency range for the Indonesian event (Fig. 4e), with amplitudes larger to the south than to the north of the suture, as for the Kuril Islands event. However, for the Indonesian event, the spectra vary rapidly inside the 0.03–0.036 Hz interval, and the main amplitude variations are located between 0.030 and 0.033 Hz. To focus on frequencies around 0.033 Hz, we show in Figs 4(b), (d) and (f) the average amplitude between 0.030 and 0.036 Hz for each station versus the distance to the suture, normalized so that the global maximum for each event is 1. For the Californian event, amplitude variations are small. For the Kuril Islands event, the stations located south of the Tsangpo Suture (white squares) show a significantly larger amplitude than the stations north of the suture (black squares). The same trend is observed for the Indonesian event. The amplitude increase between 0.030 and 0.033 Hz is somewhat hidden by the rapidly oscillating spectra and the averaging over a wider frequency interval.

The amplitude increase along the array for the Kuril Islands event indicates that these variations cannot be explained by geometrical spreading or anelastic attenuation (Fig. 4d), because the epicentral distance increases from the north to the south. Even though the waves generated by these two events

Table 2. Locations of the three events used in the spectral analysis.

	Date	Time (UT)	Latitude	Longitude	Depth (km)	M_b	M_s
California	01 Sept. 94	15:15:53,2	40.41°	−125.65°	10	6.6	7.0
Kuril Islands	04 Oct. 94	13:22:58,3	43.71°	147.33°	33	7.4	8.1
Indonesia	04 Aug. 94	22:15:37,8	−6.32°	131.54°	33	6.1	5.6

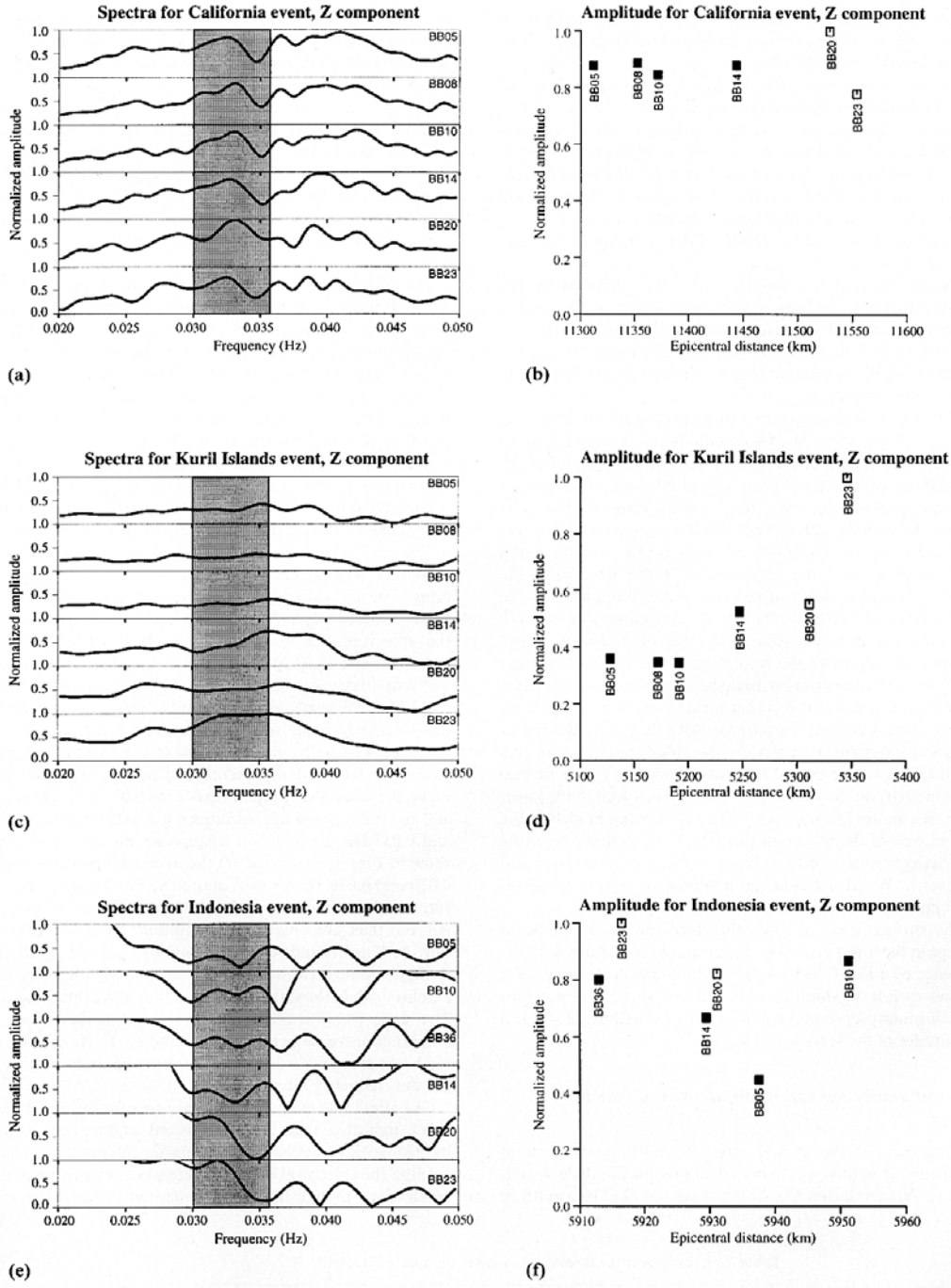

Figure 4. (a), (c), (e) Spectral amplitude for the Californian, Kuril Islands and Indonesian events recorded by broad-band stations of the INDEPTH II experiment. (b), (d), (f) Average amplitude between 0.030 and 0.036 Hz versus the distance to the Tsangpo suture for the three events. North is on the left and south is on the right. White squares are for stations located south of the suture, and black squares are for stations located north of the suture. The amplitudes are normalized as explained in the text.

are incident from opposite sides of the suture (see Fig. 1), records of the southernmost stations are always amplified with respect to records from the northern stations at a 30 s period. However, the amplitude variations are strongly dependent on backazimuth, as no amplitude variations are observed for the Californian event. A systematic observation of the azimuth dependence is not possible due to the lack of events from other backazimuths.

The amplitude variations are another indication of differences in crustal structure north and south of the Tsangpo suture but they cannot be directly inverted to obtain a velocity model. In the next section we therefore interpret these observations using forward modelling.

NUMERICAL SIMULATIONS

To investigate whether the structures found by phase velocity analysis north and south of the Tsangpo suture can explain the observed amplitude anomalies, we perform forward modelling using the indirect boundary element method (IBEM) in the formulation of Pedersen *et al.* (1996), where a plane and single mode surface wave is incident upon a multilayered and laterally heterogeneous 2-D structure. The wave can be obliquely incident upon the structure, so the wavefield is 3-D with coupling of all wave types. The calculations are performed in the frequency domain and synthetic seismograms are obtained by multiplication with a source function followed by an inverse Fourier transform.

The direction of the incident wave is defined by its 'azimuth', that is, the angle between the direction of propagation and the axis perpendicular to the structure. As the Tsangpo suture strikes E–W, the azimuth is 0° for a wave incident from the north and 180° for a wave incident from the south. The azimuth does, therefore, in the case of the Tsangpo suture, correspond to the backazimuth of the observed data.

The structure chosen for the simulations is based on phase velocity analysis. It includes a uniform upper crust and a low-velocity layer in the lower crust between 40 and 70 km north of the suture. The choice of a uniform upper crust is debatable, because the phase velocity analysis shows a difference in the upper crustal structure. We encountered numerical problems when incorporating this upper crustal variation in the model, probably due to the exponential increase of the reference solution (see Pedersen *et al.* 1996). The structure parameters are given in Table 3. As we have no information on the transition at the suture, two different models are used. As shown in Fig. 5, where the lower crustal low-velocity layer is indicated by grey shading, model 1 has a smooth transition under the suture (42 km wide), whilst model 2 has a sharp transition (3 km wide). According to our phase velocity analysis and to Chen *et al.* (1993) and Yuan *et al.* (1997), there is no indication of a change in Moho depth in this area.

All the numerical simulations are performed for the Rayleigh fundamental mode incident upon the suture. No anelastic attenuation is introduced ($Q_P = Q_S = 20\,000$). As the array north of the suture is approximately equal to the Rayleigh wavelength at a 30 s period, even a low quality factor in the low-velocity layer cannot produce significant amplitude effects within the array. Ground displacement is calculated between 0.01 and 0.1 Hz for 101 stations located between 1300 and 1700 km epicentral distance with a constant interstation distance of 4 km. The epicentral distance in the numerical

Table 3. Velocity and density parameters used for the crust north and south of the suture in the numerical simulations. d: thickness in km; V_P and V_S: P- and S-wave velocities in km s^{-1}; ρ: density in g cm^{-3}, Q_P and Q_S: quality factors for P and S waves.

North					
d (km)	V_P (km s^{-1})	V_S (km s^{-1})	ρ (g cm^{-3})	Q_P	Q_S
40.0	6.0	3.5	2.75	20 000	20 000
30.0	5.6	3.2	2.75	20 000	20 000
∞	8.1	4.6	3.20	20 000	20 000

South					
d (km)	V_P (km s^{-1})	V_S (km s^{-1})	ρ (g cm^{-3})	Q_P	Q_S
40.0	6.0	3.5	2.75	20 000	20 000
30.0	6.5	3.8	2.75	20 000	20 000
∞	8.1	4.6	3.20	20 000	20 000

simulations is the distance to the line source which produces the plane incident waves. We choose the source location so that we obtain well-dispersed waves whilst keeping the time window sufficiently short so as to avoid excessive CPU times. The measurements of spectral amplitude presented below are independent of this distance. The diffraction effects (reflection, refraction, wave conversions, etc.) and the spectral amplitudes are independent of this distance, which can therefore be chosen arbitrarily. The source function is a Ricker wavelet with a centre period of 30 s.

Fig. 6 shows the synthetic seismograms computed for the vertical component for the model with a smooth transition zone (model 1) and the model with a sharp transition zone (model 2). We simulated a Rayleigh wave incident with azimuths of 30° (Figs 6a and b), 60° (Figs 6c and d) and 120° (Figs 6e and f) to compare with the records of the Californian, Kuril Islands and Indonesian events respectively. For 30° and

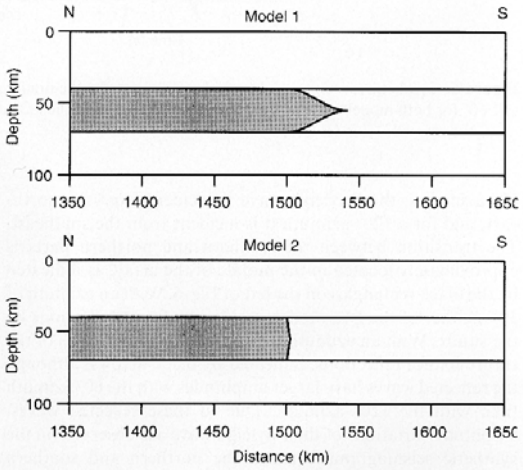

Figure 5. Models used in the numerical simulations. The grey shading shows the location of the low-velocity layer in the lower crust. Model 1 has a smooth transition (42 km wide) between the northern and southern flat-layered crusts while model 2 has a sharp transition (3 km wide).

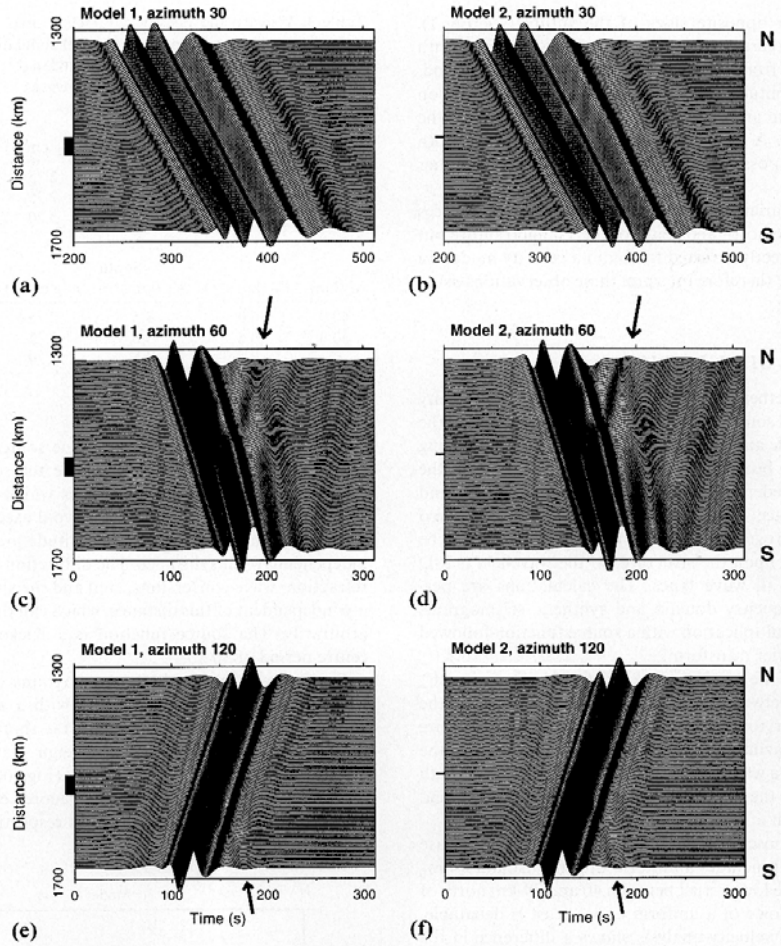

Figure 6. Synthetic seismograms (vertical component) for the fundamental mode of the Rayleigh wave incident from the north, with azimuths 30° and 60° for both models. The black rectangles correspond to the location of the transition between the northern and southern parts of the model.

60° azimuths, the Rayleigh wave is incident from the northeast, and for a 120° azimuth it is incident from the southeast. The transition between the southern and northern parts is approximately located in the middle of the array, as indicated by the black rectangles on the left of Fig. 6. With an azimuth of 30° neither of the two models yields significant reflections by the suture. With an azimuth of 60° or 120° both models of the suture induce reflections, indicated by black arrows, although the reflected waves have larger amplitudes with the 60° azimuth than with the 120° azimuth. Due to these reflected waves, amplitude variations of the Rayleigh wave are observed on the synthetic seismograms between the northern and southern parts of the suture.

The variations in the spectral amplitude of the vertical component, measured at a 30 s period for the time intervals represented in Fig. 6, are plotted as a function of epicentral distance in Fig. 7. This is the frequency where significant variations in spectral amplitude were observed across the suture (Fig. 4). The spectral amplitudes are averaged in the frequency domain using a Gaussian filter with a half-bandwidth between 0.030 and 0.036 Hz. For both models, the results for the 30° and 60° azimuths for a Rayleigh wave incident from the northeast are shown in Figs 7(a)–(d), whilst Figs 7(e) and (f) correspond to an azimuth of 120° and a wave incident from the southeast. The grey shading shows the location and the width of the transition, zones and the distances are measured as indicated in Fig. 5. Each amplitude curve is normalized by its maximum.

For a 30° azimuth (Figs 7a and b), amplitude variations are small (less than 5 per cent) and quite similar for both models. For a 60° azimuth (Figs 7c and d), amplitudes increase across the transition zone by 15 per cent for model 1 and 17.5 per cent for model 2. Strong amplitude variations due to the interferences between the incident and diffracted wavefields are

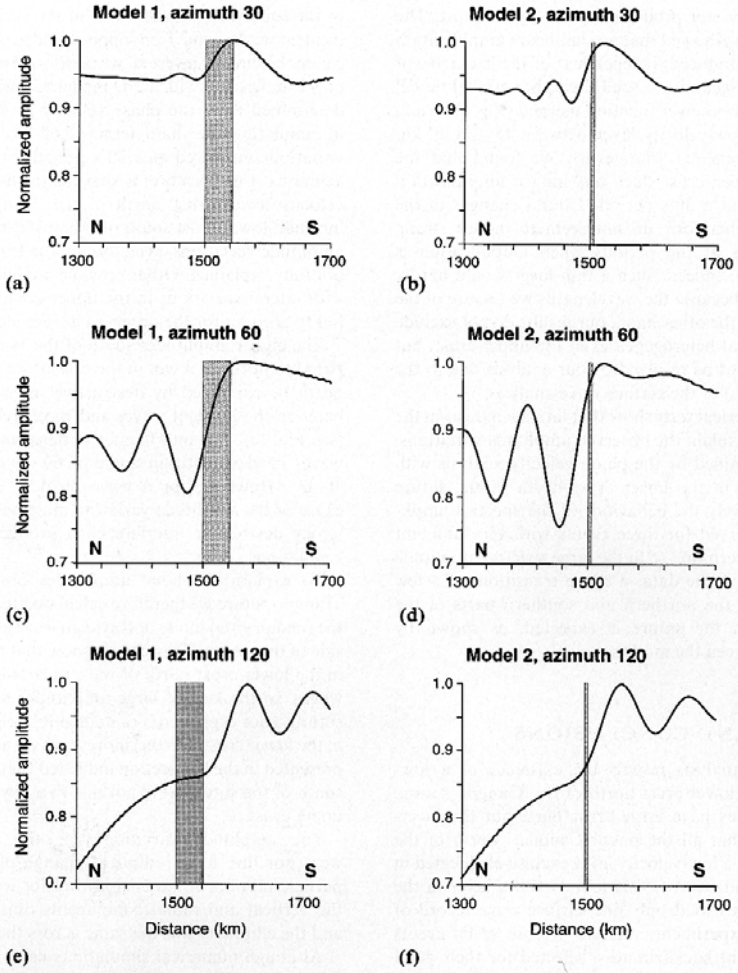

Figure 7. Amplitude variations of the vertical component at 30 s period across the array (101 stations). The grey shading shows the location of the transition between the northern and southern parts of the Tsangpo suture. (a) Model 1: 30° azimuth; (b) model 2: 30° azimuth; (c) model 1: 60° azimuth; (d) model 2: 60° azimuth; (e) model 1: 120° azimuth; (f) model 2: 120° azimuth.

also clearly visible. For a 120° azimuth (Figs 7e and f), both models give similar results. The amplitudes are larger south of the suture than north of it, like for the 60° azimuth, with an increase of approximately 20 per cent. The interference patterns have weaker amplitudes than for the 60° azimuth.

The numerical simulations show that the *S*-velocity model resulting from the phase velocity analysis and including a low-velocity layer in the lower crust north of the suture can qualitatively explain the spectral amplitude variations observed on the record of three events with very different backazimuths. With a 30° azimuth, the amplitude is quite constant across the array, as observed in data from the Californian event with a 30° backazimuth (Fig. 4a). With a 60° or 120° azimuth, amplitudes are significantly higher south of the suture than north of it, as observed in data from the Kuril Islands and Indonesian events. The amplitude profiles of Figs 4(b), (d) and (f) do not coincide with Figs 7(b), (d) and (f). However, the tendencies in the amplitude variations are the same in the numerical simulations and the observations. The amplitude difference between the southern and the northern stations is larger in the data (ratio 1.7) than in the simulations (ratio 1.2), but the variations are qualitatively the same. Finally, a comparison between a smooth transition model and a sharp transition model shows that the latter leads to higher amplitude variations, indicating that the transition beneath the suture may be as sharp as a few kilometres.

To verify that the uppermost crustal structure cannot induce significant amplitude variations at a 30 s period, we carried out another series of numerical simulations. First, we used a model with upper crustal velocities lower south than north of the suture between the surface and 6 km depth, and a homogeneous lower crust, to verify that the amplification observed

south of the suture is not produced by the upper crust. The numerical simulations showed that no significant amplification at a 30 s period was induced, independent of the geometry of the transition zone. Second, we used the upper crustal model as suggested from the receiver function method (Fig. 3b; Yuan *et al.* 1997) with a low-velocity layer between 15 and 20 km depth and a homogeneous lower crust. We found that the structure of the upper crust does not induce amplification south of the suture at a 30 s period. Lateral changes in the upper crust alone, therefore, do not seem to induce strong amplitude variations at the periods when amplification is observed in the data. Indeed, such a thin layer would hardly affect the amplitude because the wavelengths we use are of the order of 100 km. On the other hand, our results do not exclude the presence of lateral heterogeneities in the upper crust, but such structures cannot be resolved by our analysis due to the long periods (20–60 s) of the surface wave analysis.

In summary, numerical tests show that lateral changes in the upper crust cannot explain the observed amplitude variations. The structure determined by the phase velocity analysis with a low-velocity layer in the lower crust north of the suture reproduces qualitatively the behaviour of the spectral amplitude variations observed for three events with very different backazimuths. Furthermore, to fit the large spectral amplitude variations observed in the data, a sharp transition, of a few kilometres, between the northern and southern parts of the lower crust beneath the suture is expected, as shown by the comparison between the models.

DISCUSSION AND CONCLUSIONS

Our surface wave analysis reveals the existence of a low-velocity layer in the lower crust north of the Tsangpo suture. The dispersion curves have large error bars, but the inversion clearly shows that all the possible models north of the Tsangpo suture have a low-velocity layer exclusively located in the lower crust. Kind *et al.* (1996) found such a layer in the middle crust, but they used only one surface wave record of the INDEPTH II experiment, whereas we use seven events incident with different backazimuths, selected for their good signal-to-noise ratio.

Chen *et al.* (1993) presented velocity structures for different areas along and adjoining the 1991–1992 Sino–US PASSCAL experiment profile. Their results show highly varying velocity structures within southern Tibet. They find (1) a low-velocity lower crust beneath a profile located towards the northeast, (2) no low-velocity layer to the southeast beneath a profile that crosses the Tsangpo suture, and (3) no low-velocity layer beneath a profile parallel to our array, but significantly longer, sampling well into the Qiangtang terrain. Curtis & Woodhouse (1997) did not find crustal low-velocity layers in southern Tibet, but their source–station configuration did not allow for the investigation of small-scale structures.

A study of the amplitude of the Rayleigh wave fundamental mode for three different events confirms the velocity model that we have inferred from phase velocities. With a 30° backazimuth (Californian event), we do not observe amplitude variations at a 30 s period across the array. On the other hand, significant lateral variations in amplitude are observed within the array with 60° and 120° backazimuths (Kuril Islands and Indonesian events). The spectra of these records have larger amplitudes to the south than to the north of the suture, even though the incident waves come from opposite sides. As these observations cannot be directly inverted, we performed numerical simulations of 3-D diffraction with a 2-D model. Using the *S*-velocity model determined from the phase velocity inversion, we succeeded in simulating the main features of the observed amplitude variations measured at a 30 s period for 60° and 120° backazimuths. Furthermore, a sharp transition between the low-velocity lower crust north of the Tsangpo suture and the 'normal' lower crust south of it better explains observed large amplitude variations, even though the level of amplification is not fully explained. Other possible models, for example, those with lateral variations in the upper crustal velocity structure, fail to account for the observed amplitude variations.

The higher amplitudes south of the Tsangpo suture as compared to north of it can in the case of waves incident from the north be explained by destructive interference to the north between the incident waves and waves reflected on the suture (see Fig. 7b). The interference patterns are much stronger for waves incident with an angle of 60° than for those incident at 30°. However, for a wave incident from the south, the cause of the amplitude variation must be different because no strong destructive interference is produced in the numerical simulation.

To explain the large amplitudes observed south of the Tsangpo suture we therefore calculated the Eigen functions for the fundamental mode of Rayleigh wave at 30 s period for each side of the suture. They clearly show that the low-velocity layer in the lower crust north of the suture is not a trap for guided waves, so the lack of large amplitudes north of the Tsangpo suture is not explained by a guided Rayleigh wave propagating in the lower crust. Furthermore, tests on numerical simulations presented in the last section indicated that the large amplitudes south of the suture were not due to a low-velocity layer in the upper crust.

The amplitude variations for the vertical component were not due to an elliptical change of the Rayleigh wave particle motion, as no energy transfer was observed between the vertical and radial components during the propagation, and the ellipticity was the same across the array.

Although numerical simulations using the model proposed for southern Tibet explain the existence of the large-amplitude variations observed in the data, no satisfactory explanation has been found as to why large amplitudes appear exclusively south of the Tsangpo suture.

We have presented two independent arguments which indicate that there is a low-velocity layer in the lower crust north of the Tsangpo suture, and a 'normal' crust south of it. The simplest explanation for this low-*S*-wave-velocity layer (3.2 km s^{-1} between 40 and 70 km depth) is the presence of partial melt, because *S* waves are very sensitive to the presence of fluids, and their velocity decreases rapidly as the amount of fluid increases. Other seismological studies of southern Tibet (e.g. Nelson *et al.* 1996; Hirn *et al.* 1997) have also found evidence of a partially molten layer north of the Tsangpo suture, although located in the middle crust. Partial melting can be interpreted as a consequence of the anomalous thickness of the Tibetan plateau crust, induced by the shortening between the Asian and Indian plates. South of the Tsangpo suture a thermal screen due to the underthrusting of the Indian crust can be evoked to explain why there is no corresponding low-velocity anomaly south of it (Guillot & Allemand 1997).

ACKNOWLEDGMENTS

All IBEM calculations were carried out at the Centre de Calcul de l'Observatoire de Grenoble. NC was supported by the Centre National de la Recherche Scientifique and Laboratoire de Détection Géophysique contract No. 72B 087/00. We thank A. Levshin and an anonymous reviewer for constructive comments on the manuscript, and A. Paul, J. Guilbert and R. Bark for their critical reading of a preliminary version.

REFERENCES

Bourjot, L. & Romanowicz, B., 1992. Crust and upper mantle tomography in Tibet using surface waves, *Geophys. Res. Lett.*, **19,** 881–884.

Brown, L.D. *et al.*, 1996. Bright spots, structure, and magmatism in southern Tibet from INDEPTH seismic reflection profiling, *Science,* **274,** 1688–1690.

Chen, G.Y., Zeng, R.S., Wu, F.T. & Su, X.L., 1993. The phase velocities of Rayleigh waves and the lateral variation of lithospheric structure in Tibetan plateau, *Acta Seismologica Sinica,* **6,** 289–297.

Chen, L., Booker, J.R., Jones, A.G., Wu, N., Unsworth, M.J., Wei, W. & Tan, H., 1996. Electrically conductive crust in southern Tibet from INDEPTH magnetotelluric surveying, *Science,* **274,** 1694–1696.

Curtis, A. & Woodhouse, J., 1997. Crust and upper mantle shear velocity structure beneath the Tibetan plateau and surrounding regions from interevent surface wave phase velocity inversion, *J. geophys. Res.*, **102,** 11 789–11 813.

Guilbert, J., Poupinet, G. & Mei, J., 1996. A study of azimuthal P residuals and shear-wave splitting across the Kunlun range (Northern Tibetan plateau), *Phys. Earth planet. Inter.*, **95,** 167–174.

Guillot, S. & Allemand, P., 1998. Episodic tectonics of the Himalayan Belt inferred from two-dimensional thermal modelling, *Tectonophysics,* submitted.

Herrmann, R.B., 1987. *Computer Programs in Seismology,* Saint Louis University.

Hirn, A. *et al.*, 1995. Seismic anisotropy as an indicator of mantle flow beneath the Himalayas and Tibet, *Nature,* **375,** 571–574.

Hirn, A., Sapin, M., Lépine, J.-C., Diaz, J. & Mei, J., 1997. Increase in melt fraction along a south-north traverse below the Tibetan plateau: evidence from seismology, *Tectonophysics,* **273,** 17–30.

Hwang, H.J. & Mitchell, B.J., 1986. Interstation surface wave analysis by frequency-domain Wiener deconvolution and modal isolation, *Bull. seism. Soc. Am.*, **76,** 847–864.

Kind, R. *et al.*, 1996. Evidence from earthquake data for a partially molten crustal layer in southern Tibet, *Science,* **274,** 1692–1694.

Levshin, A., Ritzwoller, M. & Ratnikova, L., 1994. The nature and cause of polarization anomalies of surface waves crossing northern and central Eurasia, *Geophys. J. Int.*, **117,** 577–590.

Makovsky, Y., Klemperer, S.L., Ratschbacher, L., Brown, L.D., Li, M., Zhao, W. & Meng, F., 1996. INDEPTH wide-angle reflection observation of P-wave-to-S-wave conversion from crustal bright spots in Tibet, *Science,* **274,** 1690–1691.

McKenzie, D. & Sclater, J., 1971. The evolution of the Indian Ocean since the late Cretaceous, *Geophys. J. R. astr. Soc.*, **24,** 437–528.

McNamara, D.E., Owens, T.J. & Walter, W.R., 1996. Propagation characteristics of *Lg* across the Tibetan Plateau, *Bull. seism. Soc. Am.*, **86,** 457–469.

McNamara, D.E., Walter, W.R., Owens, T.J. & Ammon, C.J., 1997. Upper mantle velocity structure beneath the Tibetan Plateau from *Pn* travel time tomography, *J. geophys. Res.*, **102,** 493–505.

Molnar, P. & Tapponnier, P., 1975. Cenozoic tectonics of Asia: effects of a continental collision, *Science,* **189,** 421–426.

Nakanishi, I., 1979. Phase velocity and Q of mantle Rayleigh waves, *Geophys. J. R. astr. Soc.*, **58,** 35–59.

Nelson, K.D. *et al.*, 1996. Partially molten middle crust beneath southern Tibet: synthesis of project INDEPTH results, *Science,* **274,** 1684–1688.

Ni, J. & Barazangi, M., 1983. High-frequency seismic wave propagation beneath the Indian Shield, Himalayan Arc, Tibetan Plateau and surrounding regions: high uppermost mantle velocities and efficient *Sn* propagation beneath Tibet, *Geophys. J. R. astr. Soc.*, **72,** 665–689.

Pedersen, H.A., Maupin, V. & Campillo, M., 1996. Wave diffraction in multilayered media with the indirect boundary element method: application to 3-D diffraction of long-period surface waves by 2-D lithospheric structures, *Geophys. J. Int.*, **125,** 545–558.

Reese, C.C. & Ni, J., 1996. Attenuation of coda waves in southern Tibet, *Geophys. Res. Lett.*, **23,** 3015–3018.

Romanowicz, B., 1982. Constraints on the structure of the Tibet plateau from pure path phase velocities of Love and Rayleigh waves, *J. geophys. Res.*, **87,** 6865–6883.

Sandvol, E., Ni, J., Kind, R. & Zhao, W., 1997. Seismic anisotropy beneath the southern Himalayas-Tibet collision zone, *J. geophys. Res.*, **102,** 813–823.

Shapiro, N.M., Campillo, M., Paul, A., Singh, S.K., Jongmans, D. & Sanchez-Sesma, F.J., 1997. Surface-wave propagation across the Mexican Volcanic Belt and the origin of the long-period seismic-wave amplification in the valley of Mexico, *Geophys. J. Int.*, **128,** 151–166.

Taylor, S.R. & Toksöz, M.N., 1982. Measurement of interstation phase and group velocities and Q using Wiener filtering, *Bull. seism. Soc. Am.*, **72,** 73–91.

Wiener, N., 1949. *Time Series,* MIT Press, Cambridge, MA.

Wittlinger, G.F. *et al.*, 1996. Seismic tomography of northern Tibet and Kunlun: evidence for crustal blocks and mantle velocity contrasts, *Earth planet. Sci. Lett.*, **139,** 263–279.

Wu, F., Levshin, A. & Kozhevnikov, V., 1997. Rayleigh wave group velocity tomography of Siberia, China and the vicinity, *Pure appl. Geophys.*, **149,** 447–473.

Yuan, X., Ni, J., Kind, R., Mechie, J. & Sandvol, E., 1997. Lithospheric and upper mantle structure of southern Tibet from a seismological passive source experiment, *J. geophys. Res.*, **102**(B12), 27 491–27 500.

Zhao, W. *et al.*, 1997. Seismic mapping of crustal structures beneath the Indus-Yarlung Suture, Tibet, *Terra Nova,* **9,** 42–46.